KSME

Springer

Journal of Mechanical Science and Technology 39 (11) 2025

Original Article
DOI 10.1007/s12206-025-1028-1

Keywords:
· Frenet–Serret frame
· Steel wire wound
· Toroidal helical structure
· Wire-closed criterion

Correspondence to:
Jiaxuan Chen
chenjiaxuan@hit.edu.cn

Citation:
Zhang, S., Hu, S., Zhao, J., Wang, Y., Guan, X., Liu, H., Wang, L., Chen, J. (2025). Mathematical model and closure criteria for wire-wound toroidal helical structures. Journal of Mechanical Science and Technology 39 (11) (2025) 6829~6846.
https://doi.org/10.1007/s12206-025-1028-1

Received February 17th, 2025
Revised June 14th, 2025
Accepted July 3rd, 2025

† Recommended by Editor Hyun-Gyu Kim

Mathematical model and closure criteria for wire-wound toroidal helical structures

Shuai Zhang[1], Shuo Hu[1], Jiao Zhao[1], Yimeng Wang[1], Xin Guan[2], Haozhe Liu[3], Luhong Wang[4] and Jiaxuan Chen[1]

[1]School of Mechatronics Engineering, Harbin Institute of Technology, Harbin 150001, China, [2]Harbin Gongda Great Expectations Rubber and Plastic Technology Co., Ltd., Harbin 150023, China, [3]Center for High Pressure Science & Technology Advanced Research, Beijing 100094, China, [4]Shanghai Advanced Research in Physical Sciences, Shanghai 201203, China

Abstract This study establishes a mathematical model for steel wire-wound toroidal helical structures and defines a precise closure criterion. On the basis of the Frenet–Serret frame, mathematical models for single- to triple-order toroidal helices are derived. An optimized method to calculate the Frenet–Serret normal vector is proposed to substantially reduce derivation intricacy. This study proposes for the first time the mathematical modeling of single-thread winding patterns and rigorously investigates their closure criterion. Results demonstrate that the winding mechanism shares an identical criterion with multithread winding patterns. 3D software modeling by using the proposed methodology reveals enhanced accuracy in helical structure analysis. The findings provide valuable insights into the modeling of complex helical geometries.

1. Introduction

Steel wire-wound toroidal helical structures play a critical role in industries because of their excellent axial mechanical properties and radial load-carrying capacity [1-4]. The internal structure of these toroidal helical structures is crucial for their mechanical properties and service life [5-7]. Early research mainly relied on theoretical analysis and experimental testing, providing a solid foundation for subsequent scientific research and engineering applications [8-15]. With the advancement of computational technology, simulation methods have become increasingly crucial for analyzing the mechanical properties of wire-wound toroidal helical structures. Accurate mathematical and geometric models need to be constructed to ensure the reliability and validity of the simulation results [16-21].

Numerous scholars have worked to establish and optimize mathematical models for describing and predicting the mechanical behavior of helical structures. These models cover a wide range of helical structures, including straight-strand [22-25], curved-strand [26-29], and heterogeneous cross-section helices [30-33]. The most common and earliest studied structures were straight-strand helices with circular cross sections [15, 34-36]. Nawrocki and Labrosse [37] developed a finite element model for simple straight-strand helical structures by using Cartesian isoparametric expressions. Lee [34] presented various models for straight-stranded helical structures. Stanova et al. [22] and Erdönmez [23] demonstrated the derivation of mathematical models for helical structures and established models for double and triple straight-strand helices. Han et al. [19] were the first to construct a 3D model of a quadruple helix. Meanwhile, Lv et al. [38] developed a geometrically simplified analytical model for overhead transmission lines. By retaining only the corrugated geometry of the outermost armor rods and omitting the internal helical structure, this approach achieves a compromise between computational efficiency and geometric resolution. Zhao et al. [39-41] conducted a series of studies addressing the geometric modeling of complex helical structures in shearer cables. In their early work [39], the authors integrated manufacturing principles with mathematical formulations to develop a parametric 3D

model on the Pro/Engineer platform by utilizing the trajectory parameter function. This model enables parametric regulation of the lay direction, helical pitch, and inter-wire clearance, demonstrating enhanced compatibility with industrial manufacturing processes. Subsequent research [40] proposed a generalized framework for multistrand, multilayer shearer cables. By constructing geometric skeletons (i.e., steel wire centerlines) and implementing helical path control, the methodology decouples geometric modeling from load-dependent deformation stages, thereby enhancing initial configuration accuracy with structural stability. Zhao et al.'s latest work [41] established a recursive parametric modeling methodology on the Rhino–Grasshopper platform. Through curve interpolation and mesh fitting, the model captures intralayer and interlayer tangential relationships while incorporating nonstandard sheath geometries, offering flexibility for simulating complex cable structures. These studies established a comprehensive, geometrically precise modeling framework for multilayer helical shearer cables that spans path generation, structural assembly, and engineering adaptability.

During the development of helical structures, researchers have demonstrated that modifying the shape of the cross section enhances wear and torsion resistance and improves the contact state with pulley grooves [30, 33]. This insight has led to further investigations into mathematical models for helical structures with various cross-sectional shapes. Fedorko et al. [33] derived geometrical parametric equations for a two-layer helix with a triangular cross section and constructed a 3D model of the (3+9+15) structure by using Pro/Engineer software. Chen et al. [42] focused on a helical strand with an elliptical cross section, derived its parametric equations, and constructed a 3D model. Stanova et al. [30] developed a mathematical model for a wire-wound straight-strand helix with an elliptical cross section and verified it by using Pro/Engineer software. Meanwhile, Zhang et al. [31] explored mathematical models for curved-strand helical structures with elliptical and triangular cross sections and developed software to rapidly construct 3D models. Xia et al. [43] introduced a precise vector expression for the spatial trajectory of distinct steel wire types within a triangular strand-wire rope structure. Moreover, they established a parametric modeling methodology for finite element analysis using ABAQUS/CAE. The method's versatility extends to other complex rope structures, enabling the analysis of intricate strand configurations.

To minimize the effect of internal contact stresses on the service life of helical structures and enhance their strength, researchers have designed compacted steel wire helical structures. Erdönmez [44] developed a 3D model of a (1+6) compacted helical structure by analyzing the cross-sectional shape of an actual compacted wire and integrating it with parametric mathematical equations. Erdönmez [45] introduced a model for a multilayer compacted helical structure that combines the cross-sectional characteristics of a compacted steel wire with a double helix equation. Chen et al. [32] examined the process of wire compaction by using an elastoplastic mechanical model, predicted the 2D cross-sectional shape, and established a 3D model on the basis of the compacted wire cross section.

In practical applications, steel helical structures are typically bent. As a result, numerous scholars have focused on the mathematical modeling of these structures in their bent states. He et al. [29] studied bent fiber-braided ropes, derived a mathematical model, analyzed the winding process through geometric methods, and implemented a modeling approach in SolidWorks software. Ma et al. [26] developed a mathematical model for a wire rope bent around a pulley and established the corresponding helical wire core and 3D model, ultimately offering a practical approach for modeling bending helical structures. Zhang et al. [2, 46] constructed a multiorder helical model (encompassing single and double helices) for seamless closed-wire ropes and successfully facilitated a smooth transition between straight and circular arc segments. The authors also proposed methods for determining the values of characteristic parameters to ensure favorable closed-wire conditions of the toroidal helix.

These research results highlight the importance of geometric modeling for diverse and complex helical structures. Substantial progress has been made in the mathematical modeling of helical structures, and current research focuses on helices in nonclosed forms. Studies on the underlying mathematical models of wire-closed toroidal helical structures remain limited.

In this work, mathematical models of toroidal helical structures with a new winding pattern are proposed and developed for the first time, and their derivation process is optimized. The detailed mathematical models and wire-closed criteria are provided to address the gap in the research on closed helical structures. Mathematical models are presented for a range of helical winding and spiral directions for single- to triple-helix toroidal structures. Then, the mathematical models and the conditions required to ensure wire closure are validated through the construction of 3D geometries. The findings of this research not only provide a theoretical foundation for the mechanical analysis and optimal design of toroidal helical structures but also offer methodological guidance for the study of mathematical models of other types of helical structures.

2. Structural characteristics and geometric relations

2.1 Structural characteristics

A wire-wound toroidal helical structure is composed of a core wire ($n = 0$) and toroidal helical wires of various nth orders, including single ($n = 1$), double ($n = 2$), and triple ($n = 3$) helical wires. The inner schematic representation of this structure is depicted in Fig. 1(a). A single helical wire (I) is spirally wound around the surface of the core wire, forming the first layer of the helical structure known as the inner strand. The inner strand is further spirally wound by the side ropes (sr) on its surface, completing the steel wire-wound toroidal helical structure. Each side rope consists of side strands (ss) spirally wound around a single helical wire (II) in the second layer, and each side strand comprises triple helical wires wrapped around a double helical wire.

Two distinct wire-wound patterns of toroidal helical structures

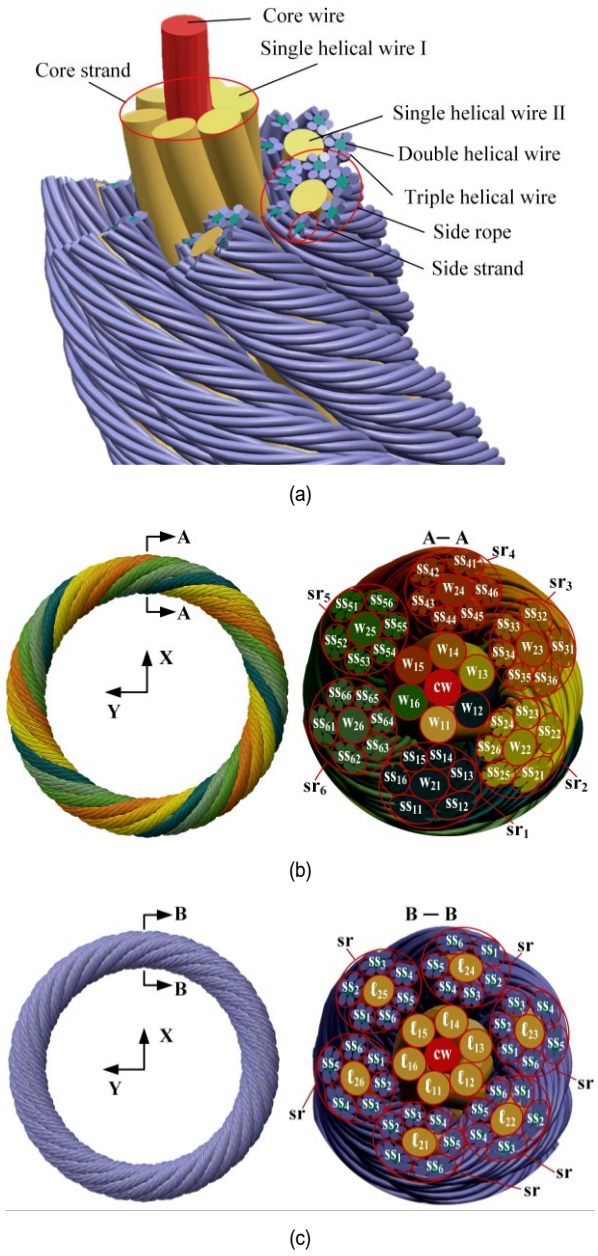

Fig. 1. Wire-wound toroidal helical structures with single- to triple-order configurations: (a) internal structure with multiorder helices; (b) multithread winding structure; (c) single-thread winding structure.

are identified: helix windings of (i) multithreads in each layer (Fig. 1(b)) and (ii) single-thread in each layer (Fig. 1(c)). In the (i) wire-wound pattern, multiple single helical wires I and side ropes are sequentially wound to form a complete toroidal structure. The single helical wires (I/II) are denoted by symbols w_{ij}, where the subscript *i* indicates the layer number (1 for single helical wire I and 2 for single helical wire II) and *j* represents the wire's serial number. The side ropes are represented by sr_j, where *j* is the serial number of the *j*th side rope corresponding to single helical wire I/II. The side strands are denoted by ss_{jk}, with *j* indicating the side rope's serial number and *k* representing the serial number of the *k*th side strand on the *j*th side rope. After completing one full revolution around the toroidal structure, the end surfaces of each helical wire align with their starting surfaces.

In the (ii) wire-wound pattern toroidal helical structure, only one single helical wire I and one side rope, which consists of six side strands and one single helical wire II, are wound back and forth to cover the entire toroidal surface. Single helical wire I and single helical wire II are denoted by ℓ_{im}, where the subscript *i* has the same definition as that in the multithread winding structure and *m* represents the serial number of the *m*th winding turn of the same wire. The side strands, which wind single helical wire II within one side rope, are represented by ss_k, with the subscript *k* indicating the serial number of the *k*th side strand. After one complete winding turn, the endpoint of single helical wire I/II is projected onto the normal plane of the core wire at a toroidal angle of $2\pi/m$, where *m* represents the number of winding turns of the wire.

2.2 Geometric relations

2.2.1 Multithread winding pattern

The geometric relationships among rotation angle, winding angle, and rotation radius are illustrated in Fig. 2.

These geometric relationships allow the establishment of the following mathematical relationship.

$$l_s = \frac{R\theta}{\cos\alpha_s} = \frac{r_s\varphi_s}{\sin\alpha_s} = \frac{r_d\varphi_d}{\tan\alpha_d}, \tag{1}$$

$$l_d = \frac{r_d\varphi_d}{\sin\alpha_d} = \frac{r_t\varphi_t}{\tan\alpha_t}. \tag{2}$$

From Eqs. (1) and (2), the relationship among θ, φ_s, φ_d, and φ_t can be deduced as follows:

$$\varphi_s = \frac{R\tan\alpha_s}{r_s}\theta, \tag{3}$$

$$\varphi_d = \frac{r_s\tan\alpha_d}{r_d\sin\alpha_s}\varphi_s, \tag{4}$$

$$\varphi_t = \frac{r_d\tan\alpha_t}{r_t\sin\alpha_d}\varphi_d. \tag{5}$$

2.2.2 Single-thread winding pattern

The most notable difference between single-thread and multithread winding methods is that after one cycle around the core wire, the head and tail of the single helical wire do not coincide but instead deviate by a certain angle. However, after *m* cycles, the head and tail align, forming a closed loop. At the end of one winding cycle, the endpoint of the center curve—located on the normal plane of the core wire's centerline—forms a central angle of $2\pi/m$ or $-2\pi/m$ with the start point on the same plane.

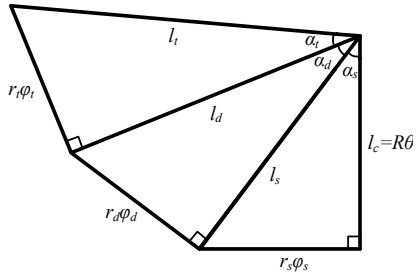

Fig. 2. Geometry of the centerline or center curve of the core, single, double, and triple helical wires.

Consequently, in a single-thread winding pattern, the values of φ'_s, φ'_d, and φ'_t are related to θ as follows:

$$\varphi'_s = \left(\frac{R\tan\alpha_s}{r_s} + \frac{1}{m} \right)\theta \,, \tag{6}$$

$$\varphi'_d = \frac{r_s \tan\alpha_d}{r_d \sin\alpha_s}\varphi'_s \,, \tag{7}$$

$$\varphi'_t = \frac{r_d \tan\alpha_t}{r_t \sin\alpha_d}\varphi'_d \,. \tag{8}$$

3. Mathematical expression of varied center curves

3.1 Fundamental principle underlying the formation of a spatial toroidal helix

Let point *A* be a point on the center curve of the *n*th-order toroidal helical wire (*n* = 0 represents the core wire, which is a non-helical structure). The (*n*+1)th-order helix is generated by spirally wrapping around the *n*th-order helix. A schematic of the spatial geometric configurations and characteristic curves is depicted in Fig. 3. Point *A* is situated on the single (*n* = 1) helix, which is employed to derive the mathematical expression of the double helix.

The unit normal, unit binormal, and unit tangent vectors at point *A* on the single helix are denoted as $\boldsymbol{n}_s$, $\boldsymbol{b}_s$, and $\boldsymbol{t}_s$, respectively. Let point *B* be a point on the (*n*+1)th-order helix, which is wound around the *n*th-order helix serving as its centerline, where point *A* is located. The position of point *A* in the Cartesian coordinate system is represented by vector $\boldsymbol{h}_s$, which points to it from the origin. The vector of point *B* within the Cartesian coordinate system is denoted as $\boldsymbol{q}_d$. Therefore, the position vector of point *B* in the Cartesian coordinate system is given by $\boldsymbol{h}_d = \boldsymbol{h}_s + \boldsymbol{q}_d$.

3.2 Centerline equation of the core wire

The centerline of the core wire (*n* = 0) is modeled as a closed circular curve, whose vector representation in the Cartesian coordinate system is given as

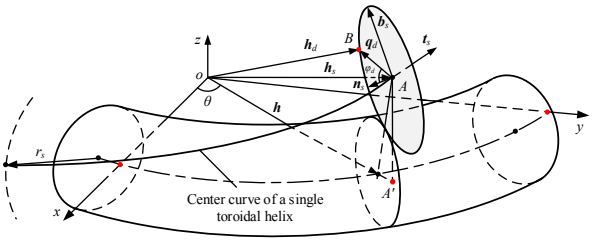

Fig. 3. Schematic of the winding formation of a double helix.

$$\boldsymbol{h} = \left(R\cos\theta, \pm R\sin\theta, 0 \right) , \tag{9}$$

where the symbol + is used when the toroidal spiral curve is formed in a counterclockwise direction and the symbol − is utilized when the spiral curve is formed in a clockwise direction.

This approach can be utilized to regulate the winding direction of the outer layer helices when the circular curve is used as the winding core.

3.3 Equation of the center curve of the single helical wire

The center curve of the single helical wire follows a single-helix trajectory formed by the superposition of two motion components: (1) axial displacement along the core wire centerline described by direction vector $\boldsymbol{h}$ (Eq. (9)) and (2) circumferential motion with rotation radius r_s and rotation angle φ_s. A Frenet–Serret moving frame, $\boldsymbol{n}_\theta$-$\boldsymbol{b}_\theta$-$\boldsymbol{t}_\theta$, is constructed along the core wire centerline to describe the circumferential motion. $\boldsymbol{t}_\theta$ is the tangent vector, $\boldsymbol{n}_\theta$ is the principal normal vector pointing toward the center of curvature, and $\boldsymbol{b}_\theta = \boldsymbol{t}_\theta \times \boldsymbol{n}_\theta$ as determined by the right-hand rule. Within this moving frame, the circumferential motion follows a circular path, and its direction vector $\boldsymbol{q}'_s$ is defined as

$$\boldsymbol{q}'_s = \left(r_s\cos\varphi_s, \pm r_s\sin\varphi_s, 0 \right) , \tag{10}$$

where the symbol + is used in the case of a right-handed spiral and the symbol − is applied for a left-handed spiral.

Given that direction vector $\boldsymbol{h}$ is defined in the global Cartesian coordinate system, whereas circumferential motion component $\boldsymbol{q}'_s$ is defined in the local Frenet–Serret moving frame, coordinate transformation is required to superimpose the two components. According to differential geometry theory, this transformation is achieved by constructing a matrix $\mathbf{T}_\theta = [\boldsymbol{n}_\theta, \boldsymbol{b}_\theta, \boldsymbol{t}_\theta]$, which transforms vector components from the local Frenet–Serret moving frame into the global coordinate system. The transformed relationship is given in Eq. (11). Such coordinate transformation ensures that both motion components (defined in different reference frames) can be consistently combined within the global Cartesian coordinate system, enabling an accurate spatial trajectory representation of the single helix.

$$\boldsymbol{q}_s = \mathbf{T}_\theta \boldsymbol{q}_s'^{\mathrm{T}} . \tag{11}$$

In accordance with differential geometry theory, transformation matrix $\mathbf{T}_\theta = [\boldsymbol{n}_\theta, \boldsymbol{b}_\theta, \boldsymbol{t}_\theta]$ is constructed from principal normal vector $\boldsymbol{n}_\theta$, binormal vector $\boldsymbol{b}_\theta$, and tangent vector $\boldsymbol{t}_\theta$, all vectors are computed as

$$\boldsymbol{t}_\theta = \frac{\boldsymbol{h}'}{|\boldsymbol{h}'|}, \boldsymbol{b}_\theta = \frac{\boldsymbol{h}' \times \boldsymbol{h}''}{|\boldsymbol{h}' \times \boldsymbol{h}''|}, \boldsymbol{n}_\theta = \boldsymbol{b}_\theta \times \boldsymbol{t}_\theta , \tag{12}$$

where $\boldsymbol{h}'$ and $\boldsymbol{h}''$ denote the first and second derivatives of vector $\boldsymbol{h}$, respectively. Their analytical expressions are given as

$$\boldsymbol{h}' = \left(-R\sin\theta, \pm R\cos\theta, 0\right), \tag{13}$$

$$\boldsymbol{h}'' = \left(-R\cos\theta, \mp R\sin\theta, 0\right). \tag{14}$$

By substituting Eqs. (13) and (14) into Eq. (12), transformation matrix $\mathbf{T}_\theta$ is explicitly derived as follows:

$$\mathbf{T}_\theta = \begin{bmatrix} -\cos\theta & 0 & -\sin\theta \\ \pm\sin\theta & 0 & \pm\cos\theta \\ 0 & \pm 1 & 0 \end{bmatrix}. \tag{15}$$

Inserting Eqs. (10) and (15) into the coordinate transformation of Eq. (11) yields the global representation of circumferential motion vector $\boldsymbol{q}_s$ as follows:

$$\boldsymbol{q}_s = \left(-r_s\cos\theta\cos\varphi_s, \pm r_s\sin\theta\cos\varphi_s, \pm r_s\sin\varphi_s\right). \tag{16}$$

By combining direction vector $\boldsymbol{h}$ with circumferential motion vector $\boldsymbol{q}_s$, the overall direction vector of the single toroidal helix is obtained as

$$\boldsymbol{h}_s = \boldsymbol{h} + \boldsymbol{q}_s . \tag{17}$$

The single helix can be classified based on the winding and spiral directions, resulting in four patterns: (i) left-handed counterclockwise winding, (ii) left-handed clockwise winding, (iii) right-handed counterclockwise winding, and (iv) right-handed clockwise winding. The operators + or − that are used to replace the ± symbols that appear in sequence in Eq. (16) corresponding to different winding patterns are shown in Table 1.

Table 1. Operators corresponding to the four types of single (n = 1) toroidal helical winding in $\boldsymbol{q}_s$.

Winding direction	Spiral direction	Operator selection: + or −	
		1	2
Counterclockwise	Left-hand	−	−
	Right-hand	−	+
Clockwise	Left-hand	+	+
	Right-hand	+	−

3.4 Equation of the center curve of the double helical wire

The formation mechanism of the double toroidal helix follows the same principle as that of the single toroidal helix. Its spatial trajectory results from the superposition of two motion components: (1) a motion along the centerline of the single toroidal helix described by direction vector $\boldsymbol{h}_s$ (Eq. (17)) and (2) a circumferential motion around the single helix trajectory characterized by rotation radius r_d and rotation angle φ_d. A Frenet–Serret moving frame, $\boldsymbol{n}_s$-$\boldsymbol{b}_s$-$\boldsymbol{t}_s$, is constructed along the centerline of the single toroidal helix to accurately represent this circumferential motion. Unit vectors $\boldsymbol{n}_s$, $\boldsymbol{b}_s$, and $\boldsymbol{t}_s$ are computed via differential geometry and used to assemble transformation matrix $\mathbf{T}_s$, which maps local vector $\boldsymbol{q}'_d$ to the global coordinate system as $\boldsymbol{q}_d$. Then, double toroidal helix direction vector $\boldsymbol{h}_d$ is obtained through vector superposition of $\boldsymbol{q}_d$ and $\boldsymbol{h}_s$.

For single- and higher-order toroidal helices, the three vectors of the Frenet–Serret frame at any point can be computed efficiently without traditional differential geometry formulas, but they can also be derived directly from geometric relations as a computationally tractable alternative. When solving for $\boldsymbol{n}_s$, the tangent vector decomposition method proposed by Østergaard [47] is partially applied, leading to a new approach that optimizes the computation of the Frenet–Serret frame's normal vector. This novel method outperforms existing methods [2, 23, 24] in terms of computational complexity and efficiency, especially when solving the mathematical expressions of high-order ($n \geq 2$) helices.

The center curve of a spatial single helical wire can be represented by two distinct tangential motion trajectories. One trajectory moves along the tangential direction of the center curve around which it is wound, and the other forms a circumferential trajectory, with motion being tangent to the formed trajectory on the normal plane of the center curve. Normal vector $\boldsymbol{n}_s$ of the spatial toroidal helix is perpendicular to the plane formed by the two tangential directions after decomposition, as shown in Fig. 4.

On the basis of this motion decomposition, an efficient methodology for constructing the Frenet–Serret frame in toroidal helices is developed. Compared with conventional differential geometry approaches, this method reduces computational cost while preserving numerical accuracy. The resulting orthonormal basis vectors are defined as

$$\boldsymbol{t}_s = \boldsymbol{t}_\theta \cos\alpha_s + \boldsymbol{t}_{\varphi_s} \sin\alpha_s, \boldsymbol{n}_s = \boldsymbol{t}_\theta \times \boldsymbol{t}_{\varphi_s}, \boldsymbol{b}_s = \boldsymbol{t}_s \times \boldsymbol{n}_s , \tag{18}$$

where $\boldsymbol{t}_\theta$ is given by Eq. (12) and $\boldsymbol{t}_{\varphi_s}$ is the normalized partial derivative of the single toroidal helix direction vector with respect to φ_s, as given in Eq. (19).

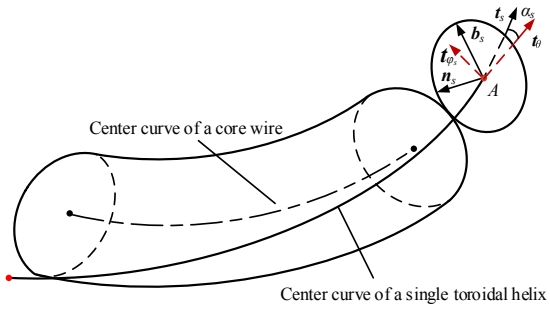

Fig. 4. Schematic of vector solving on the basis of the Frenet–Serret frame.

$$\boldsymbol{t}_{\varphi_s}=\frac{\partial \boldsymbol{h}_s(\varphi_s)}{\left|\partial \boldsymbol{h}_s(\varphi_s)\right|}=\left(\cos\theta\sin\varphi_s,\pm\sin\theta\sin\varphi_s,\pm\cos\varphi_s\right). \quad (19)$$

The three direction vectors of the Frenet–Serret frame for the single toroidal helix solution obtained using this method are given as

$$\boldsymbol{t}_s=\begin{pmatrix}\cos\theta\sin\varphi_s\sin\alpha_s-\sin\theta\cos\alpha_s;\\ \pm\cos\theta\cos\alpha_s\pm\sin\theta\sin\varphi_s\sin\alpha_s;\\ \pm\cos\varphi_s\sin\alpha_s\end{pmatrix}^{\mathrm{T}}, \quad (20)$$

$$\boldsymbol{n}_s=\begin{pmatrix}\pm\cos\theta\cos\varphi_s;\\ \pm\sin\theta\cos\varphi_s;\\ \pm\sin\varphi_s\end{pmatrix}^{\mathrm{T}}, \quad (21)$$

$$\boldsymbol{b}_s=\begin{pmatrix}-\cos\theta\sin\varphi_s\cos\alpha_s-\sin\theta\sin\alpha_s;\\ \pm\sin\theta\sin\varphi_s\cos\alpha_s\pm\cos\theta\sin\alpha_s;\\ \pm\cos\varphi_s\cos\alpha_s\end{pmatrix}^{\mathrm{T}}. \quad (22)$$

As illustrated in Fig. 4, tangent vector $\boldsymbol{t}_s$ at any point on the single toroidal helix can be decomposed into two components in accordance with the kinematics of toroidal helix formation: (1) tangent vector $\boldsymbol{t}_\theta$ of the underlying core wire centerline and (2) tangential vector $\boldsymbol{t}_{\varphi_s}$ associated with the circular winding motion on the normal plane of the core wire centerline. Given that the tangent vectors of both component motions lie on the tangent plane, the principal normal vector must be orthogonal to these tangential directions. Principal normal vector $\boldsymbol{n}_s$ is thus obtained from the cross product $\boldsymbol{t}_\theta \times \boldsymbol{t}_{\varphi_s}$.

The mathematical expression in Frenet–Serret frame $\boldsymbol{n}_s$-$\boldsymbol{b}_s$-$\boldsymbol{t}_s$ can be transformed into the Cartesian coordinate system by using a specific matrix as follows:

$$\mathbf{T}_s=\left[\boldsymbol{n}_s;\boldsymbol{b}_s;\boldsymbol{t}_s\right]^{\mathrm{T}}. \quad (23)$$

Direction vector $\boldsymbol{q}'_d$ of the circumferential motion performed by the double toroidal helix on the normal plane of the single toroidal helix, expressed in Frenet–Serret frame $\boldsymbol{n}_s$-$\boldsymbol{b}_s$-$\boldsymbol{t}_s$, is defined as

$$\boldsymbol{q}'_d=\left(r_d\cos\varphi_d,\pm r_d\sin\varphi_d,0\right), \quad (24)$$

where in the context of the spiral direction, the symbol + is used for a right-handed direction and the symbol − is used for a left-handed direction.

The expression for vector $\boldsymbol{q}_d$ in the Cartesian coordinate system is given in Eq. (25). In accordance with the toroidal helix formation principle, vector $\boldsymbol{h}_d$ of the double toroidal helix is derived in Eq. (26).

$$\boldsymbol{q}_d=\mathbf{T}_s\boldsymbol{q}'_d=\begin{pmatrix}\pm r_d\cos\theta\left(\cos\varphi_s\cos\varphi_d\right.\\ \left.\pm\sin\varphi_s\sin\varphi_d\cos\alpha_s\right)\\ \pm r_d\sin\theta\sin\varphi_d\sin\alpha_s;\\ \pm r_d\sin\theta\left(\cos\varphi_s\cos\varphi_d\right.\\ \left.\pm\sin\varphi_s\sin\varphi_d\cos\alpha_s\right)\\ \pm r_d\cos\theta\sin\varphi_d\sin\alpha_s;\\ \pm r_d\sin\varphi_s\cos\varphi_d\\ \pm r_d\cos\varphi_s\sin\varphi_d\cos\alpha_s\end{pmatrix}^{\mathrm{T}}, \quad (25)$$

$$\boldsymbol{h}_d=\boldsymbol{h}+\boldsymbol{q}_s+\boldsymbol{q}_d. \quad (26)$$

The double toroidal helix is based on the single toroidal helix as its centerline, with the spiral direction including left-handed and right-handed spirals. Given that a single toroidal helix can have four distinct winding forms, the double toroidal helix can exhibit eight distinct forms. These winding configurations are represented by specific operators in Eq. (25), as shown in detail in Table A.1 in Appendix.

3.5 Equation of the center curve of the triple helical wire

The trajectory of the triple toroidal helix comprises two motion components: axial motion along the centerline of the double toroidal helix and circumferential motion on its normal plane. Given that tangent vector $\boldsymbol{t}_d$ of the double toroidal helix centerline has been derived in the preceding section, constructing the mathematical formulation of the circumferential motion requires establishing a Frenet–Serret frame along the double toroidal helix. This process entails computing tangent vector $\boldsymbol{t}_d$, principal normal vector $\boldsymbol{n}_d$, and binormal vector $\boldsymbol{b}_d$.

On the basis of the methodology introduced, tangent vector $\boldsymbol{t}_d$ can be decomposed into two components: tangent vector $\boldsymbol{t}_s$ of the single toroidal helix and tangent vector $\boldsymbol{t}_{\varphi_d}$ associated with the circumferential motion about the single toroidal helix. Principal normal vector $\boldsymbol{n}_d$ is calculated as $\boldsymbol{t}_s \times \boldsymbol{t}_{\varphi_d}$, and binormal vector $\boldsymbol{b}_d$ is obtained from the orthogonality condition of the Frenet–Serret frame via $\boldsymbol{b}_d = \boldsymbol{t}_d \times \boldsymbol{n}_d$, as defined in Eq. (27).

$$\boldsymbol{t}_d=\boldsymbol{t}_s\cos\alpha_d+\boldsymbol{t}_{\varphi_d}\sin\alpha_d,\boldsymbol{n}_d=\boldsymbol{t}_s\times\boldsymbol{t}_{\varphi_d},\boldsymbol{b}_d=\boldsymbol{t}_s\times\boldsymbol{n}_d. \quad (27)$$

Tangent vector $\boldsymbol{t}_{\varphi_d}$ is defined as the normalized partial derivative of the double toroidal helix direction vector with respect to

angular parameter φ_d. Its computation formulation is presented as

$$\boldsymbol{t}_{\varphi_d} = \frac{\partial \boldsymbol{h}_d(\varphi_d)}{\left|\partial \boldsymbol{h}_d(\varphi_d)\right|}. \tag{28}$$

By substituting Eq. (26) into Eq. (28) and subsequently substituting Eqs. (20) and (28) into Eq. (27), the three orthonormal basis vectors of the Frenet–Serret frame along the double toroidal helix are derived, as expressed in Eqs. (29)-(31).

The vector representation in Frenet–Serret frame $\boldsymbol{n}_d$-$\boldsymbol{b}_d$-$\boldsymbol{t}_d$ can be transformed into the Cartesian coordinate system by using Eq. (32).

Direction vector $\boldsymbol{q}'_t$ of the circumferential motion performed by the triple toroidal helix on the normal plane of the double toroidal helix, expressed in Frenet–Serret frame $\boldsymbol{n}_d$-$\boldsymbol{b}_d$-$\boldsymbol{t}_d$, is defined in Eq. (33).

The calculation method for vector $\boldsymbol{q}_t$ in the Cartesian coordinate system is given in Eq. (34). The calculation method of the triple toroidal helix is derived as shown in Eq. (35).

$$\boldsymbol{n}_d = \begin{pmatrix} \sin\theta\sin\varphi_d\sin\alpha_s \\ \pm\left(\cos\varphi_d\cos\varphi_s \pm \sin\varphi_d\sin\varphi_s\cos\alpha_s\right)\cos\theta; \\ \pm\cos\theta\sin\varphi_d\sin\alpha_s \\ \pm\left(\cos\alpha_s\sin\varphi_d\sin\varphi_s \pm \cos\varphi_d\cos\varphi_s\right)\sin\theta; \\ \pm\cos\varphi_s\sin\varphi_d\cos\alpha_s \pm \sin\varphi_s\cos\varphi_d \end{pmatrix}^{\mathrm{T}}, \tag{29}$$

$$\boldsymbol{b}_d = \begin{pmatrix} \left(\begin{matrix}\pm\cos\alpha_d\sin\varphi_d\cos\varphi_s \pm \cos\alpha_s\cos\alpha_d \\ \cdot\sin\varphi_s\cos\varphi_d + \sin\alpha_s\sin\alpha_d\sin\varphi_s\end{matrix}\right)\cos\theta \\ -\left(\sin\alpha_d\cos\alpha_s \pm \sin\alpha_s\cos\alpha_d\cos\varphi_d\right)\sin\theta; \\ \pm\cos\varphi_s\cos\alpha_d\sin\theta\sin\varphi_d \pm \sin\alpha_s\cos\alpha_d \\ \cdot\cos\varphi_d\cos\theta \pm \sin\varphi_s\sin\alpha_d\sin\theta\sin\alpha_s \\ \pm\sin\alpha_d\cos\alpha_s\cos\theta \pm \cos\alpha_s\cos\alpha_d \\ \cdot\sin\theta\sin\varphi_s\cos\varphi_d; \\ \pm\cos\alpha_s\cos\alpha_d\cos\varphi_d\cos\varphi_s \pm \sin\varphi_s \\ \cdot\cos\alpha_d\sin\varphi_d \pm \sin\alpha_d\sin\alpha_s\cos\varphi_s \end{pmatrix}^{\mathrm{T}}, \tag{30}$$

$$\boldsymbol{t}_d = \begin{pmatrix} -\left(\cos\alpha_s\cos\alpha_d \pm \sin\alpha_d\sin\alpha_s\cos\varphi_d\right)\sin\theta \\ +\sin\varphi_s\sin\alpha_s\cos\alpha_d\cos\theta \\ \pm\left(\begin{matrix}\cos\varphi_s\sin\varphi_d\sin\alpha_d \\ \pm\sin\varphi_s\cos\varphi_d\sin\alpha_d\cos\alpha_s\end{matrix}\right)\cos\theta; \\ \pm\left(\cos\alpha_s\cos\alpha_d \pm \sin\alpha_s\sin\alpha_d\cos\varphi_d\right)\cos\theta \\ \pm\sin\varphi_s\sin\alpha_s\cos\alpha_d\sin\theta \\ \pm\left(\begin{matrix}\cos\varphi_s\sin\varphi_d\sin\alpha_d \pm \\ \sin\varphi_s\cos\varphi_d\sin\alpha_d\cos\alpha_s\end{matrix}\right)\sin\theta; \\ \pm\cos\varphi_s\sin\alpha_s\cos\alpha_d \\ \pm\left(\sin\varphi_s\sin\varphi_d \pm \cos\varphi_s\cos\varphi_d\cos\alpha_s\right)\sin\alpha_d \end{pmatrix}^{\mathrm{T}}, \tag{31}$$

$$\mathbf{T}_d = \left[\boldsymbol{n}_d;\boldsymbol{b}_d;\boldsymbol{t}_d\right]^{\mathrm{T}}, \tag{32}$$

$$\boldsymbol{q}'_t = \left(r_t\cos\varphi_t, \pm r_t\sin\varphi_t, 0\right), \tag{33}$$

where the operator + is used for right-handed spirals and − is for left-handed spirals.

$$\boldsymbol{q}_t = \mathbf{T}_d\boldsymbol{q}'^{\mathrm{T}}_t = \begin{pmatrix} \pm r_t\sin\varphi_t(\pm\cos\alpha_s\sin\alpha_d\sin\theta \\ \pm\cos\alpha_d\cos\varphi_s\cos\theta\sin\varphi_d \\ \pm\cos\alpha_d\cos\varphi_d\sin\alpha_s\sin\theta \\ \pm\sin\alpha_d\sin\alpha_s\cos\theta\sin\varphi_s \\ \pm\cos\alpha_d\cos\alpha_s\cos\varphi_d\cos\theta\sin\varphi_s) \\ \pm r_t\cos\varphi_t(\sin\alpha_s\sin\varphi_d\sin\theta \\ \pm\cos\varphi_d\cos\varphi_s\cos\theta \\ \pm\cos\alpha_s\cos\theta\sin\varphi_d\sin\varphi_s); \\ \pm r_t\sin\varphi_t(\pm\cos\alpha_s\sin\alpha_d\cos\theta \\ \pm\cos\alpha_d\cos\varphi_d\sin\alpha_s\cos\theta \\ \pm\cos\alpha_d\cos\varphi_s\sin\varphi_d\sin\theta \\ \pm\sin\alpha_d\sin\alpha_s\sin\varphi_s\sin\theta \\ \pm\cos\alpha_d\cos\alpha_s\cos\varphi_d\sin\varphi_s\sin\theta) \\ \pm r_t\cos\varphi_t(\pm\cos\varphi_d\cos\varphi_s\sin\theta \\ \pm\sin\alpha_s\cos\theta\sin\varphi_d \\ \pm\cos\alpha_s\sin\varphi_d\sin\varphi_s\sin\theta); \\ \pm r_t\sin\varphi_t(\pm\cos\varphi_s\sin\alpha_d\sin\alpha_s \\ \pm\cos\alpha_d\sin\varphi_d\sin\varphi_s \\ \pm\cos\alpha_d\cos\alpha_s\cos\varphi_d\cos\varphi_s) \\ \pm r_t\cos\varphi_t(\pm\cos\varphi_d\sin\varphi_s \\ \pm\cos\alpha_s\cos\varphi_s\sin\varphi_d) \end{pmatrix}^{\mathrm{T}} \tag{34}$$

$$\boldsymbol{h}_t = \boldsymbol{h} + \boldsymbol{q}_s + \boldsymbol{q}_d + \boldsymbol{q}_t. \tag{35}$$

The triple toroidal helix is based on the double toroidal helix. Given that a double toroidal helix has eight winding forms, a triple toroidal helix has 16 winding forms. These different winding forms are represented by the operators in Eq. (34), as explained in detail in Table A.2 in Appendix.

4. Wire-closed criterion of the toroidal helix

Parameterization design on the basis of the closed criterion of the winding patterns with (i) the multithread winding method and (ii) the single-thread winding method allows for the perfect closure of a toroidal helical wire of arbitrary order *n*. Two new physical parameters, spins *N* and winding circles *m*, are introduced. *N* is defined as the ratio of rotation angle φ_i of the *n*th-order helix to rotation angle φ_{i-1} of the (*n*-1)th toroidal helix that it wraps. *m* is the number of turns the wire-wound helical structure makes along the circumference of the toroid. A sufficient and necessary criterion for wire closure in the (ii) winding pattern is that $m \times N \in \mathbf{N}^+$ (i.e., $m \times N$ is a positive integer), whereas for the (i) winding pattern, the criterion is that $N \in \mathbf{N}^+$.

4.1 Closed criterion of the single helical wire

4.1.1 Multithread winding method

If the single ($n = 1$) helix formed by the multithread winding method achieves perfect closure, that is, its beginning and end align, after one complete wrap around the core wire ($n = 0$), then, in combination with Eq. (3), α_s must satisfy the following

relationship under the perfect wire-closed condition, where spin $N_s \in \mathbf{N}^+$.

$$\alpha_s = \arctan\left(\frac{r_s N_s}{R}\right). \tag{36}$$

4.1.2 Single-thread winding method

During the winding process using the single-thread winding method, when the helix completes one full cycle around the core wire ($n = 0$), spin N'_s is not an integer but includes an additional term of $1/m$. Therefore, the perfect wire-closed criterion for this winding pattern is given as

$$N'_s = \frac{\varphi'_s}{\theta} \Rightarrow \alpha_s = \arctan\left(\frac{r_s\left(mN'_s \mp 1\right)}{mR}\right), \tag{37}$$

where $N'_s = N_s \pm 1/m$, which is substituted into Eq. (37) to yield Eq. (38).

$$\alpha_s = \arctan\left(\frac{r_s\left(m\left(N_s \pm \frac{1}{m}\right) \mp 1\right)}{mR}\right) = \arctan\left(\frac{r_s N_s}{R}\right). \tag{38}$$

Therefore, the wire-closed criterion is proven to be identical for both types of winding patterns.

4.2 Closed criterion of the double helical wire

From the definition of spins N and Eq. (4), the spins of the double toroidal helix, N_d, can be calculated as

$$N_d = \frac{\varphi_d}{\varphi_s} = \frac{r_s \tan\alpha_d}{r_d \sin\alpha_s}. \tag{39}$$

Expressing r_s in Eq. (39) in terms of other parameters and substituting it into Eq. (38) yields the wire-closed criterion for the double toroidal helix as follows:

$$\alpha_d = \arctan\left(\frac{r_d N_s N_d \cos\alpha_s}{R}\right). \tag{40}$$

4.3 Closed criterion of the triple helical wire

The spins of the triple toroidal helix, N_t, can be determined via

$$N_t = \frac{\varphi_t}{\varphi_d} = \frac{r_d \tan\alpha_t}{r_t \sin\alpha_d}. \tag{41}$$

By expressing r_d in Eq. (41) in terms of other variables and substituting it into Eq. (40), the wire-closed criterion for the triple toroidal helix is obtained as

$$\alpha_t = \arctan\left(\frac{r_t N_s N_d N_t \cos\alpha_s \cos\alpha_d}{R}\right). \tag{42}$$

4.4 Theoretical improvement over existing closure criteria

Zhang et al. [2] proposed a closure criterion for multithread wound toroidal helical structures that uses radius R as the primary closure indicator. This critical parameter, R, must be an integer multiple of r_s, r_d, $\cot\alpha_d$, $\cot\alpha_s$, and $\cos\alpha_s$ (note: symbols are adapted to this work). Although this criterion enables precise closure of helical structures, it exhibits limitations. Specifically, it requires radius R to simultaneously satisfy the independent closure conditions for single and double toroidal helices (Eq. (43)). This restrictive approach substantially reduces the number of valid closure solutions.

$$\begin{cases} R = N_s r_s \cot\alpha_s \left(N_s \in \mathbf{N}^+\right) & \left(\text{Single helix}\right) \\ R = N_d r_d \cos\alpha_s \cot\alpha_d \left(N_d \in \mathbf{N}^+\right) & \left(\text{Double helix}\right) \end{cases}. \tag{43}$$

In fact, it is sufficient for radius R to satisfy a least common multiple (lcm) condition, rather than simultaneously fulfilling all individual constraints. Consequently, an optimized closure criterion based on R is proposed as follows:

$$R = K \cdot \mathrm{lcm}\left(r_s \cot\alpha_s, r_d \cos\alpha_s \cot\alpha_d\right)\left(K \in \mathbf{N}^+\right). \tag{44}$$

The optimized closure criterion based on radius R enables the effective closure of wire-wound toroidal helical structures and comprehensively incorporates all essential closure parameters. However, this criterion functions primarily as a validation-driven method for design parameters and thus lacks the incorporation of design-oriented perspectives. By contrast, the closure criterion developed in this study is intrinsically compatible with both parameter design frameworks and manufacturing logic, thus providing direct guidance for design implementation.

In practical engineering applications, key parameters, such as toroidal core radius R and wire diameter d, are determined based on the dimensional specifications and mechanical performance requirements of the target structure. The design methodologies for these parameters are beyond the scope of this study. Instead, this work focuses on determining the precise winding angle (α) under fixed parametric constraints, ensuring perfect geometric closure of toroidal helical structures. This angle-centric computational approach directly supports design and manufacturing processes and thus enhances structural reliability.

In the following section, a single toroidal helical structure is adopted as an engineering application case study to demonstrate the proposed closure criterion. Although this example focuses on the single toroidal helix configuration, the fundamental

Table 2. Structural parameters of the two-layer single-thread wound toroidal helix structure.

Parameter	Value/unit
D_{in}	267 mm
d_c	4 mm
d_1	1.55 mm
d_2	1.55 mm
m_1	10
m_2	16

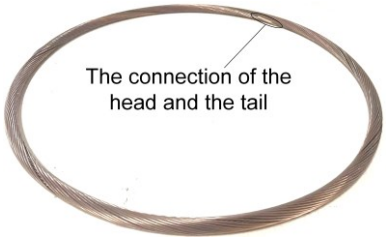

Fig. 5. Two-layer single-thread wound toroidal helical structure for tires.

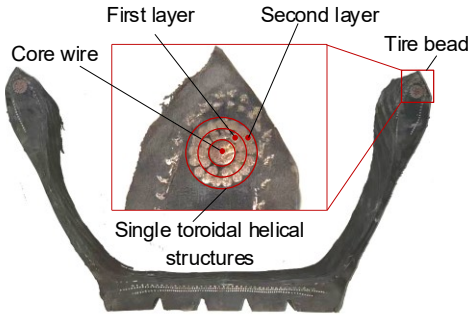

Fig. 6. Cross-sectional view of a tire.

closure principles are equally applicable to double and triple toroidal helices in practical implementations.

4.5 Application example of toroidal helical structure design

In this section, the application of the proposed closure criterion is demonstrated through an engineering case study of a single toroidal helical structure in radial tires (Fig. 5). This configuration represents a typical single-thread, multilayer, wound toroidal helix. As the core structural support of the bead section, it achieves multifunctional mechanical performance through its specialized helical architecture.

Given its unique winding configuration, this structure delivers high-stiffness reinforcement to the tire bead and enables critical load-transfer functions, including fixation, steering force transmission, and frictional engagement. Consequently, it is a key load-bearing component for ensuring the tire's operational reliability under extreme service conditions. The structural topology of the bead section is depicted in Fig. 6.

In the initial design phase of a single toroidal helical structure, the basic geometric dimensions, including nominal inner diameter D_{in} and theoretical cross-sectional diameter, are determined based on the tire's global structural requirements. Subsequently, core design variables, such as core wire diameter d_c, wire diameter d_i for each layer (with subscript i denoting the layer index), and winding turns m, are derived from these key dimensions. This derivation enables the calculation of centerline radius R and winding radii r_{si}, as shown in Eqs. (45) and (46).

$$R = \frac{D_{in}}{2} + d_1 + d_2 + \cdots + d_i + \frac{d_c}{2} \tag{45}$$

$$r_{si} = \frac{d_c}{2} + d_1 + d_2 + \cdots + d_{i-1} + \frac{d_i}{2}. \tag{46}$$

The core design parameters of the two-layer single-thread wound toroidal helix structure shown in Fig. 5 are tabulated in Table 2.

On the basis of the parameters in Table 2 and Eqs. (45) and (46), the core radius is calculated as R = 140.15 mm, and the first- and second-layer winding radii are determined as r_{s1} = 2.775 mm and r_{s2} = 4.325 mm, respectively. The closure condition (Eq. (38)) can then be used to compute winding angles α_{s1} and α_{s2} that ensure structural closure for various N_{s1} and N_{s2}. These spin parameters N are typically constrained by non-interference conditions and mechanical performance requirements (beyond this study's scope). For example, N_{s1} = 9 and N_{s2} = 8 yield closure-compliant winding angles α_{s1} = 10.10° and α_{s2} = 13.87°, respectively.

Substituting core radius R and the layer-specific parameters (r_{s1}, α_{s1}, and m_1 for the first layer and r_{s2}, α_{s2}, and m_2 for the second layer) into Eq. (6) yields the analytical relationships between polar angle φ_s and rotational angle θ for each layer under the single-thread winding pattern. Incorporating these results into the toroidal helical centerline formulation (Eq. (17)) provides the parameterized foundations for precise 3D geometric modeling of the single toroidal helical structure via CAD software.

Notably, winding angles that satisfy closure conditions are not only critical for precise geometric modeling but also serve as key control parameters in manufacturing processes. The winding angle directly determines the spatial alignment between wound and core wires during initial winding operations, influencing the structural integrity and mechanical performance of toroidal helical structures. Industrially, precise helical angle control is essential for ensuring manufacturing quality and the stability of wire-wound toroidal helices.

5. Establishment of geometric models of wire-wound toroidal helical structures

The following steps are required to model the toroidal helical

structure.

1) Select parameters for the geometry. The chosen parameters must satisfy the perfect wire-closed criteria of each *n*th-order helix listed in Sec. 4.

2) Define the parameters and input the mathematical expression of each helix.

3) Establish the center curve of each helix.

4) Generate each wire-wound toroidal helical structure model by sweeping the established center curve as a guide line and the corresponding circular curve as a generatrix.

The wire-closed criterion and the parametric expressions for each order of the toroidal helical structure are employed to generate 3D models of the wire-wound (i) multithread and (ii) single-thread toroidal helical structures, which are presented in Figs. 7 and 8, respectively. Fig. 9 illustrates the validation for the winding and spiral directions, it includes 16 combinations of the forms.

5.1 Multithread winding pattern

Fig. 7 comprehensively illustrates the hierarchical modeling process for multithread wound toroidal helical structures, thereby validating the proposed mathematical model of the multithread winding method. The modeling begins by constructing a circular core wire of radius R (Fig. 7(a)), whose spatial configuration is governed by Eq. (9).

Subsequently, six single helical wires—denoted as w_{11} to w_{16}—are generated to form the first layer (Figs. 7(b) and 7(c)). Each wire is wound with radius r_{s1}. Its spatial trajectory is governed by Eq. (17), and the initial phase angle of the jth wire is set to $(j\text{-}1)\xi_{sd1}$.

The second layer employs a compound helical winding pattern integrating single to triple helices. The base element comprises a central single helical wire (Fig. 7(d), Eq. (17), winding radius r_{s2}). With the first side strand as an exemplar, it integrates a double central helix (Fig. 7(e), Eq. (26), winding radius r_d) and a triple outer helix (Fig. 7(f), Eq. (35), winding radius r_t). The initial phase angle of the jth triple helix is set to $(j\text{-}1)\xi_t$. The complete configuration of the side strand is presented in Fig. 7(g).

Replicating this modeling process for each side strand yields the complete side rope assembly (Fig. 7(h)), and the initial phase angle of the double central helix in the jth side strand is defined as $(j\text{-}1)\xi_d$. Sequentially generating all side ropes by using this method completes the full multithread wound toroidal helical structure model (Fig. 7(i)), where the initial phase angle of the central helix in the jth side rope is $(j\text{-}1)\xi_{s2}$. The angular rotation relationships are governed by Eqs. (3)–(5).

5.2 Single-thread winding pattern

Fig. 8 illustrates the modeling process for single-thread wound toroidal helical structures. The construction of the circular core wire (radius R) follows the methodology established in Section 5.1 (Fig. 8(a)). The first layer is formed by a reciprocating single helical wire governed by Eq. (17) with winding radius r_{s1}, as shown in Fig. 8(b).

The second layer implements the same composite winding pattern that integrates single to triple helices constructed via a single side rope. This rope comprises (1) a central single helical wire (Fig. 8(c), Eq. (17), winding radius r_{s2}); (2) six side strands, each containing one double helical wire (Fig. 8(d), Eq. (26), winding radius r_d); and (3) six triple helical wires (Fig. 8(e), Eq. (35), winding radius r_t).

Fig. 8(f) displays the geometry of the first side strand, with the initial phase angle of the jth triple helix being set to $(j\text{-}1)\xi_t$. Replicating this modeling process for each side strand assembles the complete structure, yielding the final configuration shown in Fig. 8(g). The initial phase angle of the double helix in the jth side strand is defined as $(j\text{-}1)\xi_d$.

Notably, when modeling single-thread wound toroidal helical structures, rotational angle variables φ_s, φ_d, and φ_t in Eqs. (17), (26), and (35) must be replaced with their modified counterparts φ'_s, φ'_d, and φ'_t, respectively. The relationships among these adjusted rotation angles are governed by Eqs. (6)–(8).

5.3 Validation of the winding and spiral direction regulation model

Sixteen sets of 3D visualization models are constructed to intuitively demonstrate the proposed mathematical model's capability to regulate winding and spiral directions (Fig. 9). These models, which are based on the side rope structure, incorporate single, double, and triple helical wires. The model's versatility and controllability are comprehensively validated by systematically permuting the spiral direction at each helical level and the side rope's winding direction about the core wire.

Given that the directional control logic of multithread and single-thread winding methods are fundamentally consistent, the analysis in this section focuses on the multithread winding method for simplification.

Structurally, each side rope comprises three hierarchically nested helices: a triple helix that winds around a double helix to form a side strand and multiple side strands that wind around a single helix to form the side rope. The entire assembly is then wound along the toroidal core surface to achieve a closed-loop configuration.

This nested architecture enables independent left- or right-handed orientation adoption at each helical level (single, double, and triple), and the side rope can wind clockwise or counterclockwise around the core wire. Helix handedness across the three levels and the winding direction yield 16 possible configurations, which theoretically encompass all feasible directional permutations.

Fig. 9 systematically presents all 16 configurations incorporating triple helices organized by side rope winding direction and internal helical handedness. In each subfigure, the red arrows indicate the side rope winding direction, and the yellow, green, and purple arrows represent the handedness of single, double, and triple helices, respectively.

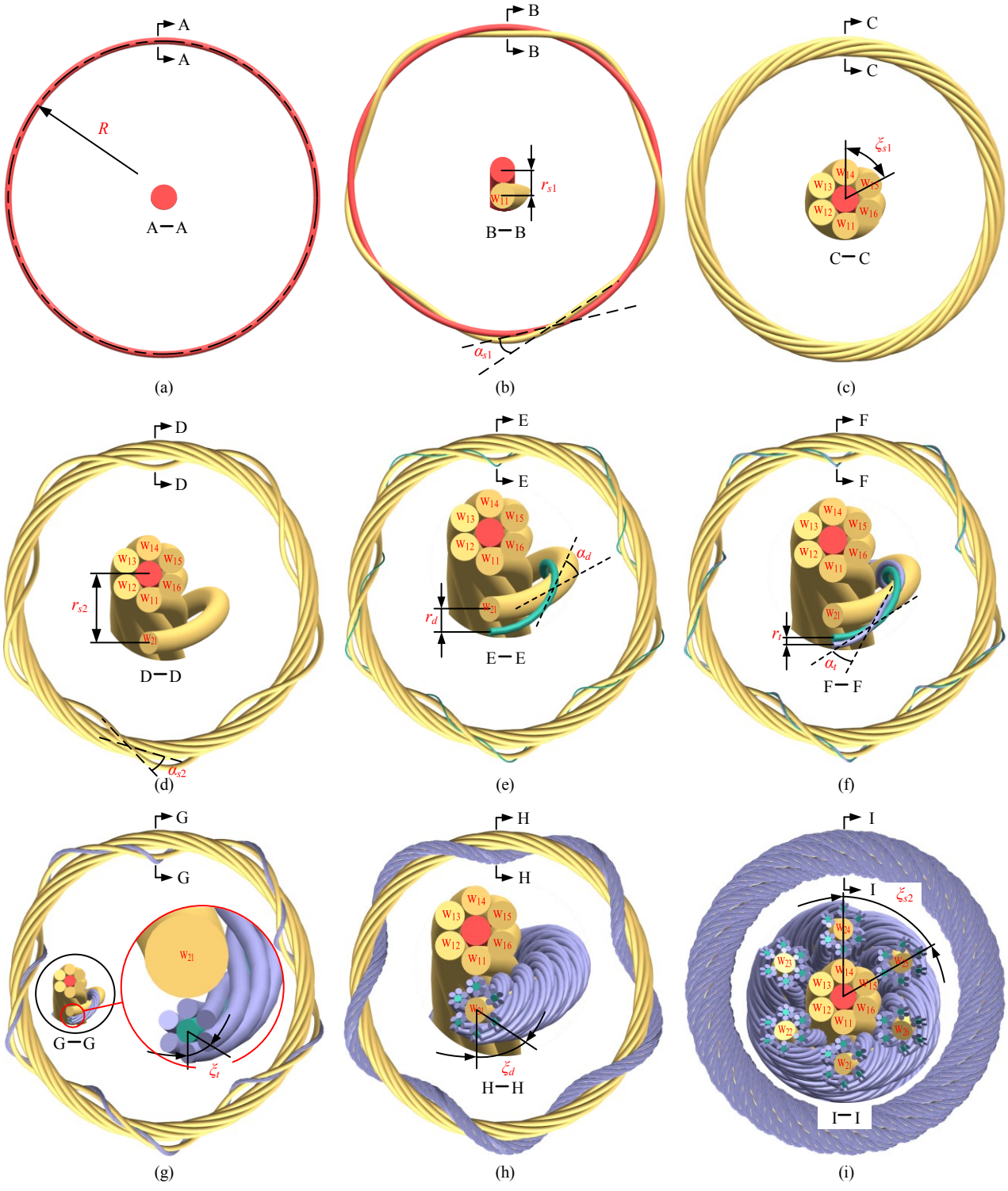

Fig. 7. Modeling of a wire-wound toroidal helical structure with a multithread winding pattern: (a) core wire model; (b) first helical wire in the first layer; (c) complete first-layer helical wire set (six wires); (d) single helical wire in the second layer; (e) first double helical wire in the second layer; (f) first triple helical wire in the second layer; (g) first side strand model in the second layer; (h) first side rope model in the second layer; (i) complete multithread wound model. The insets show cross-sectional views highlighting the internal configurations.

Figs. 9(a)-(h) illustrate eight configurations with counterclockwise winding around the core wire, ranging from all-left-handed helices (Fig. 9(a)) to all-right-handed helices (Fig. 9(h)) and encompassing all intermediate helical handedness permutations.

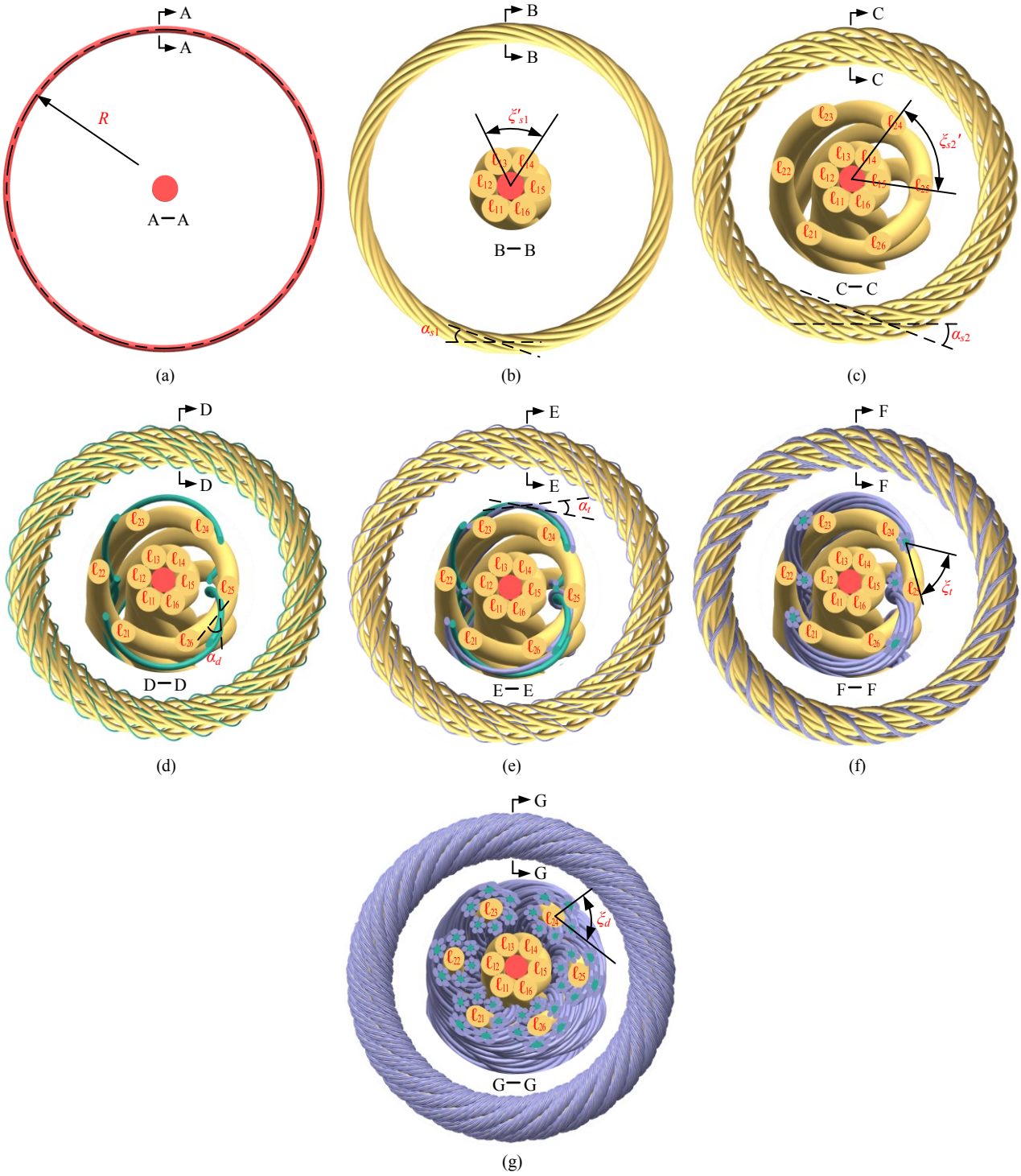

Fig. 8. Modeling of a wire-wound toroidal helical structure by using the single-thread winding pattern: (a) core wire model; (b) first-layer single helical wire model; (c) second-layer single helical wire model; (d) second-layer double helical wire model; (e) first triple helical wire in the second layer; (f) first side strand model in the second layer; (g) complete single-thread wound model. The insets show cross-sectional views of the internal structure.

Figs. 9(i)–(p) show identical helical handedness combinations but reverse the winding direction to clockwise, providing a complete comparative set of spatial configurations.

For visual clarity, noncritical structures are rendered transparent to emphasize the spatial relationships between the side ropes and the core wire, along with multiorder helical orientations. The visualization results demonstrate the mathematical model's precise generation of any desired winding–spiral direc-

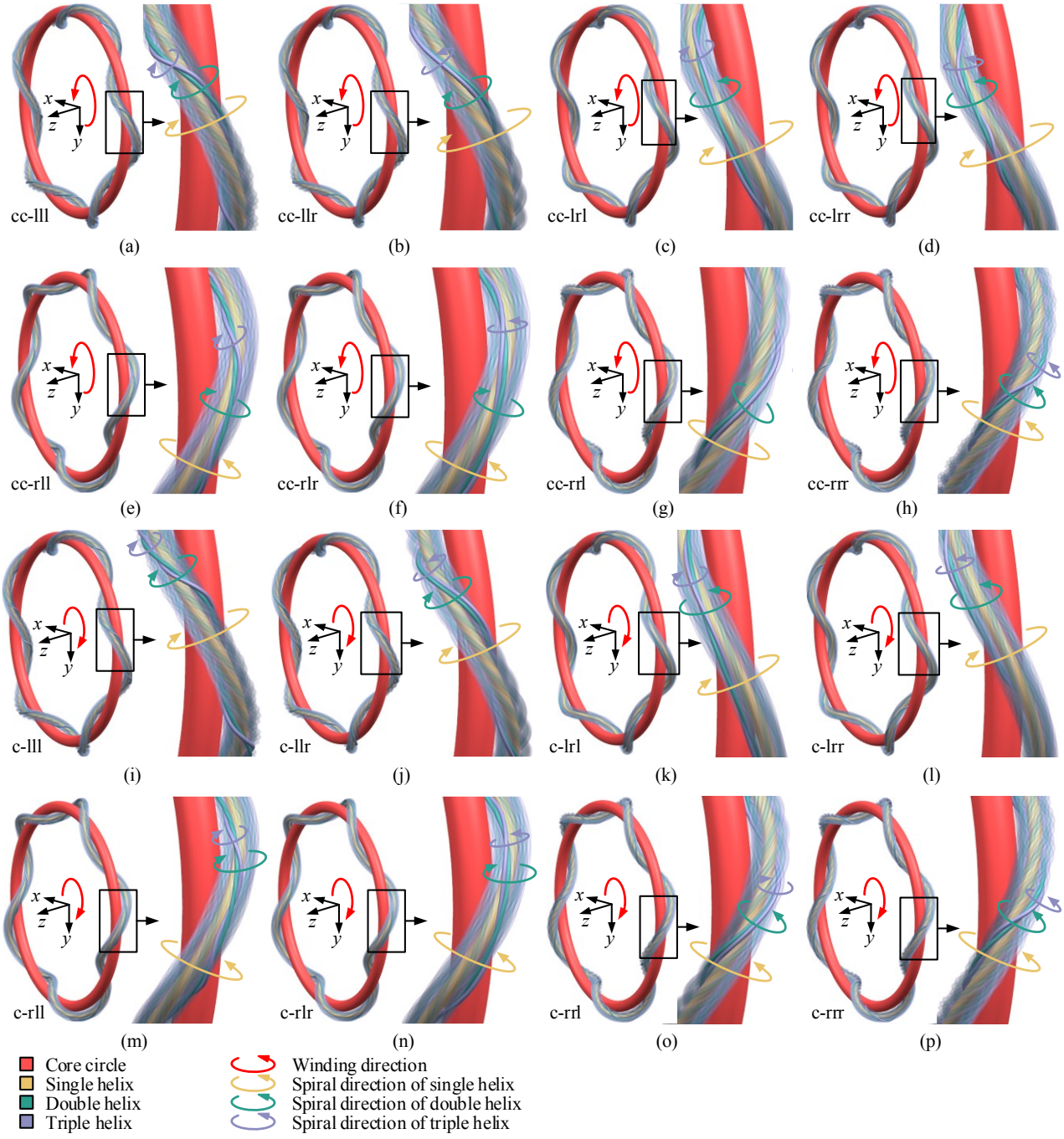

Fig. 9. 3D verification model of the winding and spiral directions of a varied-order wire-wound helix, where the letters in the lower-left corner of each subfigure indicate different combinations of winding and spiral directions. The letter preceding the symbol "–" represents the winding direction, the letter following "–" represents the spiral direction, and the letters representing the spiral direction denote single, double, and triple helices in sequence. The letters "cc" and "c" denote counterclockwise and clockwise winding directions, respectively. The letters "l" and "r" indicate left- and right-handed spiral directions, respectively. One spiral steel wire with an obvious winding relationship and one core wire are selected to enhance the clarity of the spiral direction. These steel wires are set to be opaque. All other wires are set to be translucent for an enhanced view.

tion combination under given parameters, validating its robust applicability and fine-grained controllability in designing complex multiorder helical structures.

The research results presented above demonstrate the accuracy of the mathematical and geometric model, wire-closed criterion, winding direction, and spiral direction of each order of the helix derived in this work. Moreover, the accuracy of the proposed methodology for deriving the mathematical expressions of the helix and the optimization computation method for the Frenet–Serret frame vectors is validated.

6. Conclusions

An accurate mathematical model is essential for the mechanical analysis of helical structures. The use of such a model to establish a precise geometric model is crucial for ensuring the accuracy of finite element analysis results. This study investigates the mathematical models of various wire-wound toroidal helical structures, and the main conclusions are as follows:

1) An optimized method for calculating the normal vector in the Frenet–Serret frame is proposed. This method facilitates the derivation and construction of a mathematical model for a triple (n = 3) helix structure, providing a powerful tool for in-depth studies on the mechanical and dynamic properties of toroidal helix structures.
2) Toroidal helical structures formed by two different winding patterns are constructed. Notably, the single-thread winding method for each layer of helical structures is introduced for the first time, thus opening new avenues for research on helical structures.
3) Investigation of the wire-closed criterion for (i) multithread and (ii) single-thread wound toroidal helical structures demonstrates that the closure criteria for both winding patterns are consistent. 3D models incorporating single, double, and triple wire-wound toroidal helical structures are successfully established, providing a solid theoretical foundation for the accurate design and fabrication of these structures.

This study proposes precise mathematical models and provides corresponding closure criteria for achieving perfect geometric closure. However, the current model lacks evaluation criteria for contact states between adjacent interlayer wires. Consequently, it cannot assess packing density in single-layer wire arrangements, imposing limitations on parameter design guidance. Future research should develop parameter design methods that are based on adjacent wire spacing within the same toroidal helical layer. This approach will prevent interference from excessive wire density (a common cause of finite element analysis nonconvergence) while avoiding mechanical performance degradation due to oversized gaps. Integrating these spacing-based methods with the proposed models and closure criteria will establish a comprehensive theoretical foundation for parameter design and geometric construction of wire-wound toroidal helical structures.

Acknowledgments

This work was supported by the Central Government-Guided Local Science and Technology Development Funds Project (ZY23CG10), the China Higher Education Institution Industry-University-Research Innovation Fund (2022IT044), the Heilongjiang Province Key Research and Development Plan Project (2022ZX03A04), and the HIT-CMCC 5G Application Innovation Joint Institute Fund (2023B004).

Conflict of interest

The authors declare no competing interests.

Nomenclature

A : An arbitrary point on the center curve of the nth-order helical core wire
B : An arbitrary point on the center curve of the (n+1)th-order helical core wire
l_c : Arc length of the (n=0) core wire centerline
l_s : Length of the single (n=1) helix
l_d : Length of the double (n=2) helix
l_t : Length of the triple (n=3) helix
R : Radius of the core wire centerline
r_s : Winding radius of the single helix
r_{si} : Winding radius of the ith-layer single helix
r_d : Winding radius of the double helix
r_t : Winding radius of the triple helix
θ : Rotation angle of the core wire centerline
α_s : Spiral angle of the single helix
α_d : Spiral angle of the double helix
α_t : Spiral angle of the triple helix
φ_s : Rotation angle of single helix turns around the core wire centerline
φ_d : Rotation angle of double helix turns around the single helix
φ_t : Rotation angle of triple helix turns around the double helix
φ'_s : Rotation angle of single helix turns around the core wire centerline at a single-thread winding pattern
φ'_d : Rotation angle of double helix turns around the single helix at a single-thread winding pattern
φ'_t : Rotation angle of triple helix turns around the double helix at a single-thread winding pattern
m : In winding circles, number of turns the toroidal helix winds around the z axis
N : Within one winding circle, number of complete rotations of a helix turning around its centerline
N_s : Number of spins of the single helix
N_d : Number of spins of the double helix
N_t : Number of spins of the triple helix
$\boldsymbol{n}_\theta$: Unit normal vector of the core wire centerline
$\boldsymbol{n}_s$: Unit normal vector of the single helix
$\boldsymbol{n}_d$: Unit normal vector of the double helix
$\boldsymbol{b}_\theta$: Unit binormal vector of the core wire centerline
$\boldsymbol{b}_s$: Unit binormal vector of the single helix
$\boldsymbol{b}_d$: Unit binormal vector of the double helix
$\boldsymbol{t}_\theta$: Unit tangent vector of the core wire centerline
$\boldsymbol{t}_s$: Unit tangent vector of the single helix
$\boldsymbol{t}_d$: Unit tangent vector of the double helix
$\boldsymbol{t}_{\varphi_s}$: Unit tangent vector of partial motions on the normal plane of the core wire centerline
$\boldsymbol{t}_{\varphi_d}$: Unit tangent vector of partial motions on the normal plane of the single helix
$\boldsymbol{h}$: Vector representation of the core wire centerline
$\boldsymbol{h}_s$: Vector representation of the single helix

$\boldsymbol{h}_d$: Vector representation of the double helix
$\boldsymbol{h}_t$: Vector representation of the triple helix
$\partial \boldsymbol{h}_s(\varphi_s)$: Partial differentiation of vector representation of the single helix with respect to φ_s
$\partial \boldsymbol{h}_d(\varphi_d)$: Partial differentiation of vector representation of the double helix with respect to φ_d
$\boldsymbol{q}'_s$: Vector representation of the single helix in the Frenet–Serret frame of the core wire centerline
$\boldsymbol{q}'_d$: Vector representation of the double helix in the Frenet–Serret frame of the single helix
$\boldsymbol{q}'_t$: Vector representation of the triple helix in the Frenet–Serret frame of the double helix
$\boldsymbol{q}_s$: Vector representation of the single helix in the Cartesian coordinate system
$\boldsymbol{q}_d$: Vector representation of the double helix in the Cartesian coordinate system
$\boldsymbol{q}_t$: Vector representation of the triple helix in the Cartesian coordinate system
$\boldsymbol{T}_\theta$: Transformation matrix from the Frenet–Serret frame of the core wire centerline to the Cartesian coordinate system
$\boldsymbol{T}_s$: Transformation matrix from the Frenet–Serret frame of the single helix to the Cartesian coordinate system
$\boldsymbol{T}_d$: Transformation matrix from the Frenet–Serret frame of the double helix to the Cartesian coordinate system
ξ_{si} : Multithread in each layer winding pattern: initial phase angle difference between neighboring single helices in the *i*th-layer
ξ_d : Multithread in each layer winding pattern: initial phase angle difference between neighboring double helices
ξ_t : Multithread in each layer winding pattern: initial phase angle difference between neighboring triple helices
ξ'_{si} : Single thread in each layer winding pattern: in the *i*th-layer, phase angle difference between neighboring single helices formed by winding two circles of the same wire on the centerline
ξ'_d : Single thread in each layer winding pattern: in the *i*th-layer, phase angle difference between neighboring double helices
ξ'_t : Single thread in each layer winding pattern: in the *i*th-layer, phase angle difference between neighboring triple helices
D_{in} : Normal inner diameter of toroidal helical structures
d_c : Core wire diameter
d_i : Wire diameter in the *i*th layer

References

[1] F. Wang, H. J. Chang, B. H. Ma, Y. G. Wang, L. M. Yang, J. Liu and X. L. Dong, Flexible guided anti-collision device for bridge pier protection against ship collision: Numerical simulation and ship collision field test, *Ocean Engineering*, 271 (2023) 113696, https://doi.org/10.1016/j.oceaneng.2023.113696.

[2] W. Zhang, X. Q. Zhang, C. W. Zhang, Z. X. Lu and J. F. Zhang, Geometric modeling theory and 3D solid implementation of closed wire rope on Pro/E, *Journal of the Brazilian Society of Mechanical Sciences and Engineering*, 42 (8) (2020) 391, https://doi.org/10.1007/s40430-020-02480-6.

[3] Y. Li, X. Sun, J. L. Song, S. D. Zhang and S. L. Han, Topological structure and experimental investigation of a novel whole tire bead, *Materials & Design*, 203 (2021) 109592, https://doi.org/10.1016/j.matdes.2021.109592.

[4] C. Marin-Artieda and A. Pardo-Ramos, Energy dissipation enhancement of wire rope isolators, *Results in Engineering*, 22 (2024) 102154, https://doi.org/10.1016/j.rineng.2024.102154.

[5] M. Fraldi, G. Perrella, M. Ciervo, F. Bosia and N. M. Pugno, A hybrid deterministic-probabilistic approach to model the mechanical response of helically arranged hierarchical strands, *Journal of the Mechanics and Physics of Solids*, 106 (2017) 338-352, https://doi.org/10.1016/j.jmps.2017.05.013.

[6] A. Cutolo, A. R. Carotenuto, S. Palumbo, F. Bosia, N. M. Pugno and M. Fraldi, Unveiling a new shear stress transfer mechanism in composites with helically wound hierarchical fibres, *International Journal of Mechanical Sciences*, 192 (2021) 106135, https://doi.org/10.1016/j.ijmecsci.2020.106135.

[7] Y. Ma, B. Shi, L. Ali, Y. Bai and P. Fang, Mechanical analysis of a type of wire rope subjected to tension, *Ships and Offshore Structures*, 19 (4) (2024) 541-547, https://doi.org/10.1080/17445302.2023.2190445.

[8] R. H. Knapp, Derivation of a new stiffness matrix for helically armoured cables considering tension and torsion, *International Journal for Numerical Methods in Engineering*, 14 (1979) 515-529, https://doi.org/10.1002/nme.1620140405.

[9] K. G. McConnell and W. P. Zemke, A model to predict the coupled axial torsion properties of ACSR electrical conductors, *Experimental Mechanics*, 22 (7) (1982) 237-244, https://doi.org/10.1007/BF02326388.

[10] W. S. Utting and N. Jones, Tensile testing of a wire rope strand, *The Journal of Strain Analysis for Engineering Design*, 20 (3) (1985) 151-164, https://doi.org/10.1243/03093247V203151.

[11] J. W. Phillips and G. A. Costello, Analysis of wire ropes with internal-wire-rope cores, *Journal of Applied Mechanics*, 52 (3) (1985) 510-516, https://doi.org/10.1115/1.3169092.

[12] W. S. Utting and N. Jones, The response of wire rope strands to axial tensile loads—Part II. Comparison of experimental results and theoretical predictions, *International Journal of* Mechanical *Sciences*, 29 (9) (1987) 621-636, https://doi.org/10. 1016/0020-7403(87)90034-8.

[13] M. Raoof and Y. P. Huang, Wire stress calculations in helical strands undergoing bending, *Journal of Offshore Mechanics and Arctic Engineering*, 114 (3) (1992) 212-219, https://doi.org/10.1115/1.2919973.

[14] A. Cardou and C. Jolicoeur, Mechanical models of helical strands, *Applied Mechanics Reviews*, 50 (1) (1997) 1-14, https://doi.org/10.1115/1.3101684.

[15] R. H. Knapp, Nonlinear analysis of a helically armored cable with nonuniform mechanical properties in tension and torsion, *OCEAN 75 Conference*, IEEE (1975) 155-164, https://doi.org/10.1109/OCEANS.1975.1154154.

[16] W. G. Jiang, J. L. Henshall and J. M. Walton, A concise finite element model for three-layered straight wire rope strand, *Inter-*

national Journal of Mechanical Sciences, 42 (1) (2000) 63-86, https://doi.org/10.1016/S0020-7403(98)00111-8.

[17] H. Usabiaga and J. M. Pagalday, Analytical procedure for modelling recursively and wire by wire stranded ropes subjected to traction and torsion loads, *International Journal of Solids and Structures*, 45 (21) (2008) 5503-5520, https://doi.org/10.1016/j.ijsolstr.2008.04.009.

[18] W. J. Zhang, X. F. Yuan, C. Chen and L. Yang, Finite element analysis of steel wire ropes considering creep and analysis of influencing factors of creep, *Engineering Structures*, 229 (2021) 111665, https://doi.org/10.1016/j.engstruct.2020.111665.

[19] Y. C. Han, H. D. Yong and Y. H. Zhou, The global mechanical response and local contact in multilevel helical structures under axial tension, *International Journal of Mechanical Sciences*, 239 (2023) 107886, https://doi.org/10.1016/j.ijmecsci.2022.107886.

[20] E. A. W. D. Menezes and R. J. Marczak, Comparative analysis of different approaches for computing axial, torsional and bending stiffnesses of cables and wire ropes, *Engineering Structures*, 241 (2021) 112487, https://doi.org/10.1016/j.engstruct.2021.112487.

[21] R. Judge, Z. Yang, S. W. Jones and G. Beattie, Full 3D finite element modelling of spiral strand cables, *Construction and Building Materials*, 35 (2012) 452-459, https://doi.org/10.1016/j.conbuildmat.2011.12.073.

[22] E. Stanova, G. Fedorko, M. Fabian and S. Kmet, Computer modelling of wire strands and ropes Part I: Theory and computer implementation, *Advances in Engineering Software*, 42 (6) (2011) 305-315, https://doi.org/10.1016/j.advengsoft.2011.02.008.

[23] C. Erdönmez, n-tuple complex helical geometry modeling using parametric equations, *Engineering with Computers*, 30 (4) (2014) 715-726, https://doi.org/10.1007/s00366-013-0319-9.

[24] P. Zhang, M. L. Duan, J. M. Ma and Y. Zhang, A precise mathematical model for geometric modeling of wire rope strands structure, *Applied Mathematical Modelling*, 76 (2019) 151-171, https://doi.org/10.1016/j.apm.2019.06.005.

[25] L. Xiang, H. Y. Wang, Y. Chen, Y. J. Guan, Y. L. Wang and L. H. Dai, Modeling of multi-strand wire ropes subjected to axial tension and torsion loads, *International Journal of Solids and Structures*, 58 (2015) 233-246, https://doi.org/10.1016/j.ijsolstr.2015.01.007.

[26] W. Ma, Z. C. Zhu, Y. X. Peng and G. A. Chen, Computer-aided modeling of wire ropes bent over a sheave, *Advances in Engineering Software*, 90 (2015) 11-21, https://doi.org/10.1016/j.advengsoft.2015.06.006.

[27] X. Y. Wang, X. B. Meng, J. X. Wang, Y. H. Sun and K. Gao, Mathematical modeling and geometric analysis for wire rope strands, *Applied Mathematical Modelling*, 39 (3-4) (2015) 1019-1032, https://doi.org/10.1016/j.apm.2014.07.015.

[28] W. Zhang, C. W. Zhang, W. Guo, X. B. Xu and Z. X. Lu, Research on modeling and bending stress distribution of a new metal belt continuously variable transmission, *Mechanism and Machine Theory*, 116 (2017) 220-233, https://doi.org/10.1016/j.mechmachtheory.2017.05.022.

[29] G. F. He, C. F. Sheng, H. W. He, R. Zhou, D. Yuan, X. Ning and F. G. Ning, Mathematical and geometrical modeling of braided ropes bent over a sheave, *Journal of Engineered Fibers and Fabrics*, 15 (2020) 1-13, https://doi.org/10.1177/1558925020939726.

[30] E. Stanova, G. Fedorko, S. Kmet, V. Molnar and M. Fabian, Finite element analysis of spiral strands with different shapes subjected to axial loads, *Advances in Engineering Software*, 83 (2015) 45-58, https://doi.org/10.1016/j.advengsoft.2015.01.004.

[31] W. Zhang, C. Lv, W. Liu, X. Zhang and F. Han, Modeling theory and rapid parameterized implementation of a circular arc wire rope with a special-shaped cross section, *Journal of Mechanical Science and Technology*, 36 (4) (2022) 1761-1769, https://doi.org/10.1007/s12206-022-0312-6.

[32] L. Chen, M. Magliulo, M. Elig and L. Beex, A mechanical model for compaction of strands for wire ropes, *International Journal of Solids and Structures*, 269 (2023) 112178, https://doi.org/10.1016/ j.ijsolstr.2023.112178.

[33] G. Fedorko, E. Stanova, V. Molnar, N. Husakova and S. Kmet, Computer modelling and finite element analysis of spiral triangular strands, *Advances in Engineering Software*, 73 (2014) 11-21, https://doi.org/10.1016/j.advengsoft.2014.02.004.

[34] W. K. Lee, An insight into wire rope geometry, *International Journal of Solids and Structures*, 28 (4) (1991) 471-490, https://doi.org/10.1016/0020-7683(91)90060-S.

[35] S. Machida and A. Durelli, Response of a strand to axial and torsional displacements, *Journal of Mechanical Engineering Science*, 15 (4) (1973) 241-251, https://doi.org/10.1243/JMES_JOUR_1973_015_045_02.

[36] M. Imran, D. Wang and M. A. Wahab, Three-dimensional finite element simulations of fretting wear in steel wires used in coal mine hoisting system, *Advances in Engineering Software*, 184 (2023) 103499, https://doi.org/10.1016/j.advengsoft.2023.103499.

[37] A. Nawrocki and M. Labrosse, A finite element model for simple straight wire rope strands, *Computers & Structures*, 77 (4) (2000) 345-359, https://doi.org/10.1016/S0045-7949(00)00026-2.

[38] Z. B. Lv, G. H. Liu, F. Y. Li, C. Wu, Y. G. Tao, J. F. Liu, Z. F. Ye, X. H. Liu, Y. T. Sun and Y. Bo, Study on the fastening characteristics of pre-formed helical fittings considering the surface effect of transmission lines, *Scientific Reports*, 13 (1) (2023) 10928, https://doi.org/10.1038/s41598-023-36982-9.

[39] L. J. Zhao, T. Zhang, J. Gu, T. X. Wang, B. Xie and F. Gao, N-level complex helical structure modeling method, *Scientific Reports*, 14 (1) (2024) 18549, https://doi.org/10.1038/s41598-024-69246-1.

[40] L. J. Zhao, H. N. Zhang, F. Gao, L. G. Han and M. Ge, Research on dynamic characteristics of large deformation shearer cable based on absolute node coordinate formulation method, *PLoS One*, 18 (2) (2023) e0281136, https://doi.org/10.1371/journal.pone.0281136.

[41] L. J. Zhao, H. N. Zhang, F. Gao and S. J. Yang, Research on parameterized modeling and mechanical characteristics of shearer cables, *PLOS One*, 19 (5) (2024) e0304007, https://doi.org/10.1371/journal.pone.0304007.

[42] Y. P. Chen, F. M. Meng and X. S. Gong, Parametric modeling and comparative finite element analysis of spiral triangular strand and simple straight strand, *Advances in Engineering Software*, 90 (2015) 63-75, https://doi.org/10.1016/j.advengsoft.2015.06.011.

[43] Y. F. Xia, L. Deng, X. J. Chen, C. N. Jia, Z. D. Yang, J. S. Zhu, X.

Zhang, P. Wang and D. Z. Li, Parametric modeling and finite element analysis of triangular strand wire rope, *Engineering Structures*, 314 (2024) 118398, https://doi.org/10.1016/j.engstruct.2024.118398.

[44] C. Erdönmez, Computational design of the compacted wire strand model and its behavior under axial elongation, *International Journal of Precision Engineering and Manufacturing*, 20 (11) (2019) 1957-1968, https://doi.org/10.1007/s12541-019-00204-y.

[45] C. Erdönmez, Analysis and design of compacted IWRC meshed model under axial strain, *International Journal of Mechanics and Materials in Design*, 16 (3) (2019) 647-661, https://doi.org/10.1007/s10999-019-09481-x.

[46] W. Zhang, X. Zhang, C. Zhang and J. Zhang, Theory and implementation of no-joint wire rope spatial geometry modeling, *Mathematical Problems in Engineering*, 2019 (1) (2019) 8760578, https://doi.org/10.1155/2019/8760578.

[47] N. H. Østergaard, A. Lyckegaard and J. H. Andreasen, A method for prediction of the equilibrium state of a long and slender wire on a frictionless toroid applied for analysis of flexible pipe structures, *Engineering Structures*, 34 (2012) 391-399, https://doi.org/10.1016/j.engstruct.2011.10.012.

Appendix

The + or − symbols in the table indicate the appropriate operators for the ± symbols that appear in sequence in the corresponding mathematical expressions with different winding and spiral directions. L stands for left-hand, and R stands for right-hand.

Table A.1. Operators corresponding to the eight types of double (n = 2) toroidal helical winding in $\boldsymbol{q}_d$.

Winding direction	Spiral direction		Operator selection: + or −							
			qd							
			x			y			z	
	Single toroidal helix	Double toroidal helix	1	2	3	1	2	3	1	2
Counterclockwise	L	L	-	-	+	-	-	-	-	-
		R	-	+	-	-	+	+	-	+
	R	L	+	+	+	+	+	-	-	+
		R	+	-	-	+	-	+	-	-
Clockwise	L	L	-	-	+	+	-	+	+	+
		R	-	+	-	+	+	-	+	-
	R	L	+	+	+	-	+	+	+	-
		R	+	-	-	-	-	-	+	+

Table A.2. Operators corresponding to the 16 types of triple (n = 3) toroidal helical winding in $\boldsymbol{q}_t$.

Winding direction			Counterclockwise								Clockwise							
Single toroidal helix			L				R				L				R			
Double toroidal helix			L		R		L		R		L		R		L		R	
Triple toroidal helix			L	R	L	R	L	R	L	R	L	R	L	R	L	R	L	R
Operator selection: + or −	x	1	+	-	-	+	+	-	-	+	+	-	-	+	+	-	-	+
		2	+	+	-	-	+	+	-	-	+	+	-	-	+	+	-	-
		3	+	+	-	-	-	-	+	+	+	+	-	-	-	-	+	+
		4	+	+	+	+	+	+	+	+	+	+	+	+	+	+	+	+
		5	-	-	+	+	-	-	+	+	-	-	+	+	-	-	+	+
		6	+	+	+	+	+	+	+	+	+	+	+	+	+	+	+	+
		7	+	+	+	+	+	+	+	+	+	+	+	+	+	+	+	+
		8	+	+	+	+	+	+	+	+	+	+	+	+	+	+	+	+
		9	-	-	+	+	+	+	-	-	-	-	+	+	+	+	-	-
		10	+	+	+	+	+	+	+	+	+	+	+	+	+	+	+	+
	y	1	-	+	-	+	-	+	-	+	+	-	+	-	+	-	+	-
		2	+	+	+	+	+	+	+	+	+	+	+	+	+	+	+	+
		3	+	+	-	-	+	+	-	-	+	+	-	-	+	+	-	-
		4	-	-	-	-	+	+	+	+	-	-	-	-	+	+	+	+
		5	+	+	+	+	+	+	+	+	+	+	+	+	+	+	+	+
		6	-	-	+	+	-	-	+	+	-	-	+	+	-	-	+	+
		7	-	-	+	+	+	+	-	-	+	+	-	-	-	-	+	+
		8	+	+	+	+	+	+	+	+	+	+	+	+	+	+	+	+
		9	+	+	-	-	-	-	+	+	+	+	-	-	-	-	+	+
		10	-	-	+	+	+	+	-	-	-	-	+	+	+	+	-	-
	z_t	1	+	-	+	-	+	-	-	+	-	+	-	+	-	+	+	-
		2	+	+	+	+	-	-	+	+	+	+	+	+	-	-	+	+
		3	+	+	+	+	+	+	-	-	+	+	+	+	+	+	-	-
		4	-	-	+	+	+	+	+	+	-	-	+	+	+	+	+	+
		5	-	-	+	+	-	-	+	+	+	+	-	-	+	+	-	-
		6	+	+	+	+	+	+	+	+	+	+	+	+	+	+	+	+
		7	+	+	-	-	-	-	+	+	+	+	-	-	-	-	+	+

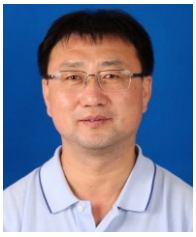

Jiaxuan Chen is a Professor at the School of Mechatronics Engineering, Harbin Institute of Technology, Harbin, China. He received his Ph.D. in Mechanical Engineering from Harbin Institute of Technology. His research interests include ultra-precision processing and nanotechnology, ultra-clean precision design and manufacturing technology, precision automatic equipment technology, winding technology, rubber and plastic technology, and automatic equipment.